Insight into the Effect of Dealumination on Mordenite Using Experimentally Validated Simulations

S. Ban,[†] A. N. C. van Laak,[‡] J. Landers,[§] A. V. Neimark,[§] P. E. de Jongh,[‡] K. P. de Jong,[‡] and T. J. H. Vlugt*,[∥]

Condensed Matter and Interfaces, Department of Chemistry, Utrecht University, P.O. Box 80.000, 3508 TA Utrecht, The Netherlands, Inorganic Chemistry and Catalysis, Department of Chemistry, Utrecht University, P.O. Box 80.000, 3508 TA Utrecht, The Netherlands, Department of Chemical and Biochemical Engineering, Rutgers, The State University of New Jersey, 98 Brett Road, Piscataway, New Jersey 08854-8058, and Process & Energy Laboratory, Delft University of Technology, Leeghwaterstraat 44, 2628 CA Delft, The Netherlands

Received: October 15, 2009; Revised Manuscript Received: December 10, 2009

Mordenite (MOR-type zeolite) is a widely used catalyst, in particular for (hydro-) isomerization and alkylation reactions in the petrochemical industry. However, having a one-dimensional micropore system, this material is susceptible to diffusion limitations and deactivation. To circumvent this problem, typically additional (meso)porosity is created by applying dealumination and/or steaming processes. The detailed description of the dealumination process is of crucial importance to understand how mordenite can be modified into an efficient catalyst. In this work, we present for the first time a simulation model to describe the influence of the dealumination process on the structural properties of mordenite. Using kinetic Monte Carlo simulations, dealumination is described as a multiple-step process consisting of the removal of the framework Al as well as the self-healing of silanol nests by Si atoms. The simulation results are in very good agreement with experimental results from ^{29}Si NMR, XRD, and N_2 and Ar physisorption. In particular, the simulations confirm the enlargement of the micropores and the creation of mesopores during dealumination.

1. Introduction

Materials with hierarchical pore systems are of importance in fields such as catalysis, adsorption and drug delivery.[1] Zeolites are prime examples, in particular those zeolites that combine micropores with mesopores, often referred to as mesoporous zeolites.[2−5] Mesopores are essential to improve the mass transfer characteristics of microporous zeolite crystals. Recently, several new methods to obtain mesoporous zeolites have been developed such as bifunctional templating,[6] carbon templating[7−9] and desilication.[10,11] However, dealumination prevails as the method of choice for zeolite modification to arrive at mesoporosity.[4] Steaming and/or acid leaching of zeolites is used to bring about the desired extent of dealumination.

Mordenite (MOR-type zeolite) is a widely used catalyst, most importantly for cracking, (hydro-) isomerization, and alkylation reactions in the petrochemical industry.[12−16] This zeolite contains one-dimensional straight channels along the *z* crystallographic axis, usually referred to as main channels, with twelve-membered rings of 6.5 × 7.0 Å. The main channels are interconnected by side pockets via eight-membered rings (3.4 × 4.8 Å) along the *y* crystallographic axis. These side pockets are inaccessible to molecules larger than methane.[17,18] As a result of the effectively one-dimensional micropore system, mordenite is susceptible to diffusion limitations and deactivation. To circumvent this problem, typically additional (meso)porosity is created by applying dealumination and/or steaming processes.[19,12,15,20−23] These processes change both the acidity and the porosity. The number of Brønsted acid sites, directly related to the number of the framework Al atoms, is being reduced. However, the acid strength of the remaining Brønsted acid sites increases, at least up to a certain Si/Al ratio.[24,25] Another factor is the change in porosity. Nagano et al.[22] showed that dealumination of mordenite leads to an enlargement of the main channels and, even more pronounced, the side pockets. Furthermore, dealumination can create additional mesoporosity. Due to the improved diffusion properties and higher resistance to deactivation, dealuminated mordenite has been proposed for many industrial applications.[12,14,15] It is of crucial importance to understand how framework Al is distributed over the zeolite framework, and whether and how this is changed upon dealumination. There are indications that it is possible to preferentially leach Al from specific positions,[23,26] especially from the side pockets. This will have an important impact not only on the size and connectivity of the additionally created pores, but also on the location of the active acid sites for catalysis.

Although dealumination of zeolites is of eminent importance, the molecular details of this process are not well understood. A few model descriptions have been reported in literature. Sokol et al.[27] used density function theory to study local framework defects generated by dealumination. Although individual defects are accurately studied on the atomic scale, the changes of the zeolite porosity cannot be extracted from their work. Ding et al.[28] adopted Monte Carlo simulations to study the Si−Al connectivity for parent and dealuminated MOR and compared the results with those of ^{29}Si NMR experiments. This approach only focuses on the Al distribution without considering the structure of the MOR framework explicitly. In order to be able to describe the dealumination process, and its impact on the Al distribution, crystallinity, Si/Al ratio, and porosity, we present

* Corresponding author. E-mail: t.j.h.vlugt@tudelft.nl.
[†] Condensed Matter and Interfaces, Department of Chemistry, Utrecht University.
[‡] Inorganic Chemistry and Catalysis, Department of Chemistry, Utrecht University.
[§] Rutgers, The State University of New Jersey.
[∥] Delft University of Technology.

10.1021/jp909900a
Published on Web 01/19/2010

in this paper kinetic Monte Carlo simulations of the dealumination process. First, the framework Al distribution in the simulation is compared to ^{29}Si NMR experiments from literature. Validity of the simulated framework is also provided by a comparison of the simulated and experimental XRD patterns. Second, the dealumination process is described using kinetic Monte Carlo simulations, providing access to the resulting changes in Si−Al connectivity (directly determining the acidity of the Brønsted acid sites), crystallinity, porosity, and pore size distribution. The good agreement between simulation and available experimental data support the validity of our detailed description of the dealumination process. By combining experiments and simulations a more detailed picture can be obtained than is accessible experimentally.

2. Methods

2.1. Sample Preparation. Sodium mordenite supplied by Albemarle Catalysts was ion-exchanged in an aqueous 1 M ammonium nitrate solution at 353 K for 24 h, followed by filtering and washing. Per gram of mordenite 12 mL of ammonia nitrate solution was used. This procedure was repeated twice to ensure complete removal of sodium ions. The sample was then converted from the ammonia form to the proton form by heating to 723 K with a ramp of 1 K/min and a dwell time of three hours. The obtained mordenite sample had a Si/Al ratio of 6. This sample will be referred to as A6 (parent mordenite). The dealuminated MOR was obtained by treating the parent sample for one hour at 100 °C in 6 M HNO_3 followed by calcination at 450 °C for three hours. After repeating this procedure twice, a mordenite sample with a Si/Al ratio of 50 was obtained. This sample will be referred to as A50.

2.2. Crystallinity. Crystal size and morphology were determined with a Tecnai FEI XL 30SFEG Scanning Electron Microscope (SEM). For A6 and A50 HMOR samples, powder X-ray diffraction (XRD) patterns were obtained using a Bruker-AS D8 with Co Kα radiation ($\lambda = 0.1789$ nm) in the range of 5°∼40° (2θ). In this work, the crystallinity is defined as the sum of the intensities of the [330], [150], [241], [202], [350], and [511] diffraction planes, normalized by assuming that this sum for the parent HMOR corresponds to 100% crystallinity.[14] XRD patterns were calculated from simulations using a MOR supercell containing 28 × 25 × 68 unit cells, in the absence of water molecules. A Lorentzian distribution was assumed for the calculated XRD intensities.[29] The full width at half of the maximum intensity was set to 0.08° (2θ). Note that experimentally XRD usually yields diffraction patterns with broader lines due to instrumental broadening, disorder, and/or small crystallite sizes. The isotropic displacement factors are set to 2.5 Å for Si and Al atoms and 5.1 Å for O atoms. To calculate the XRD pattern only scattering by the framework atoms (Si, Al, and O) is taken into account, as the scattering contributions of the protons can be neglected.[30]

2.3. Porosity. Experimentally the porosity was studied using N_2 and Ar physisorption. N_2 physisorption isotherms were recorded with a Micromeritics Tristar 3000 at a constant temperature of 77 K. Prior to the physisorption measurements, the samples were dried overnight at 573 K in a flow of nitrogen. The *t*-plot method was applied to obtain the micropore volumes and external surface areas. To accurately study the microporosity, Ar physisorption was performed. These measurements were performed at a constant temperature of 87 K with an Autosorb-1-C instrument (Quantachrome Instruments) equipped with a high precision pressure transducer (Baratron MKS), which allowed for low pressure measurements in the range of 0.0133−133 Pa. The saturation pressure p_0 was measured throughout the entire analysis by means of a dedicated saturation pressure transducer. Low-pressure data points were corrected for the thermal transpiration effect according to a standard procedure.[31] Prior to the adsorption analysis, the samples were outgassed at 573 K for 3 h.

Ar adsorption isotherms were analyzed using non-local density functional theory (NLDFT) that allows for the quantification of both micro- and mesopores.[32−35] The NLDFT models have been shown to accurately describe pore size distributions in silica materials that exhibit cylindrical and spherical mesopores, and they have been extended to the micropore region with a lower limit of around 4.5 Å.[34,35] The pore size distribution has been obtained from the adsorption branch of the isotherm by the hybrid NLDFT kernel composed of metastable adsorption isotherms in spheroidal pores larger than 50 Å and equilibrium adsorption isotherms in cylindrical pores smaller than 50 Å.[35] Thus, this model assumes a representation of the pore network as a system of spheroidal shaped mesopores connected by cylindrical channels, and embedded in a microporous matrix; the micropore shape is assumed cylindrical as well. This assumption seems plausible for mordenite. This hybrid kernel accurately describes the delay of condensation in mesoscopic voids in the region of adsorption hysteresis and the reversible equilibrium adsorption in micropores and small connecting mesopores.

In the computer simulations, the porosity is computed using a geometric method originally developed to calculate zeolite microporosities.[36] The size of a pore is defined as the maximum diameter of a sphere that fits in the pore. This definition is generally applicable to all pores with an arbitrary structure. The size distribution of the pores is computed as follows: (1) a three-dimensional grid is constructed. (2) A sphere is positioned at a random position. The radius of this sphere is set as the minimum distance between the center of the sphere and any of the zeolite framework atoms, minus the radius of the closest framework atom. (3) The radius of the sphere is recorded for all grid points inside this sphere. (4) This procedure is repeated many times. For each grid point, the maximum radius of the sphere is recorded. The simulation stops when the maximum radius for each grid point is converged. (5) The fraction of pores with a radius between r and $r + \Delta r$ is equal to the fraction of grid points belonging to spheres with a maximum radius between r and $r + \Delta r$. From this, the pore size distribution $p(r)$ can be computed in units of mL g^{-1} Å^{-1}. The total pore volume follows from the integration of $p(r)$. In N_2/Ar physisorption experiments, the smallest pore that can be detected is larger than 4.5 Å.[37] Electron tomography does not show mesopores larger than 100 Å.[38] We hence compute the total pore volume by integration of $p(r)$ from 4.5 to 100 Å. Note that even though the standard IUPAC classification defines micropores as pores smaller than 20 Å, here it is more natural to define micropores as pores smaller than 8 Å.

2.4. Initial Location of Framework Al. The framework of mordenite can be constructed using only 5-1 secondary building units,[39] forming 4, 5, 8, and 12-membered rings.[39] Each unit cell $T_{48}O_{96}$ contains four distinctly different tetrahedral sites T_1, T_2, T_3, and T_4 and 10 distinct oxygen sites O_1 through O_{10}. The four-membered rings (four per unit cell) each contain two T_3 and two T_4 sites. The T_3 and T_4 sites are located near the side pockets, while the T_1 and T_2 sites can be found in the main channel, see also ref 36. For a more detailed description of the structure and symmetry of mordenite, we refer the reader to refs 39 and 40 The early study of Alberti et al.[40] showed that in HMOR, the Al relative content of the T sites has a ratio of

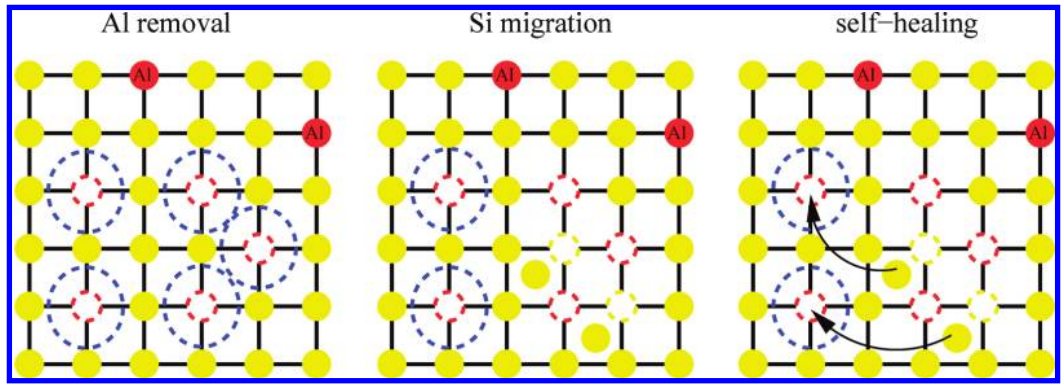

Figure 1. Schematic representation of the dealumination scheme used in the simulations: Al removal (Al−), Si migration (Si−), and self-healing (Si+), see section 2.5. Mordenite is schematically represented by an orthogonal lattice, where framework Al is denoted by red spheres and framework Si by yellow spheres. The removed Al and migrated Si atoms are drawn as dashed red and yellow circles, respectively. Silanol nests are indicated as blue dashed circles. The arrows show the self-healing of silanol nests by migrated Si atoms. Nearly all migrated Si atoms are used for this.

T_1:T_2:T_3:T_4 = 18:10:43:29 for a wide range of the Si/Al ratio. Furthermore, the Brønsted acid sites are preferentially located at O_2, O_7 and O_9. As each unit cell of MOR contains 16 T_1 atoms, 16 T_2 atoms, 8 T_3 atoms and 8 T_4 atoms, the total number of Al atoms present at each T site scales as T_1:T_2:T_3:T_4 = 36:20:43:29 the number of T_1 and T_2 sites is twice as large as the number of T_3 and T_4 sites). This result agrees well with quantum mechanical calculations[41−44] that show the preferential occupancy of Al at the four-membered rings of MOR. This is also in agreement with results of molecular simulations.[45,46]

In this work, we constructed a supercell consisting of 28 × 25 × 68 unit cells, i.e., a = 506.6 Å, b = 512.9 Å, and c = 511.6 Å, starting from an all-silica mordenite. In the model, the Al−O bond length is considered equal to the Si−O bond length. For a given Si/Al ratio, a Monte Carlo (MC) scheme is used to distribute the Al atoms over the framework, using the relative Al occupancy at each T site derived by Alberti et al.[40] Initially, the T sites for Al are randomly selected, in such a way that two Al atoms are separated by at least one Si atom in order to obey the Löwenstein rule. Based on electrostatic arguments, Dempsey et al.[47] proposed that the number of Al−O−Si−O−Al linkages has to be minimized for a given Si/Al ratio. However, Schröder et al.[48] and Limtrakul et al.[49,50] showed that Dempsey's rule does not hold for zeolites with multiple four-membered rings, which is supported by the experiments of Takaishi et al.[51] In this paper, we propose that Dempsey's rule applies to all Al except for Al in four-membered rings i.e. T_3 and T_4 sites.

The distribution of Al in the framework is simulated using a Monte Carlo (MC) simulation. We considered the interaction of a next-nearest-neighboring Al pair in the Al−O−Si−O−Al linkage. The energy of this pair is given by E_{ij} (in units of k_BT), where i and j are the indexes of the T sites of Al (i, j = 1,...4, note that $E_{ij} = E_{ji}$). Here, E_{34} is set to a negative value as the Al−O−Si−O−Al linkage is favored at the T_3 and T_4 sites of four-membered rings. The other E_{ij} are set to large positive values ($\gg|E_{34}|$) as according to Dempsey's rule the Al−O−Si−O−Al linkage should be avoided at other T sites. In each MC step, an attempt is made to exchange the position of a randomly selected framework Al with a framework Si atom. This move is accepted when the total energy is lowered, otherwise it is rejected. Configurations that violate Löwenstein's rule are always rejected. A typical simulation requires at least 10^4 trial moves for each Al atom.

We also created stacking fault domains in the MOR framework. Experimentally it has been shown that mordenite crystals consist of unit cells of *Cmcm* symmetry interdispersed with unit cells that are offset by half a unit cell along the z crystallographic axis.[52] Such packing defects are often referred to as the stacking faults. XRD refinements show that mordenite samples may contain up to 20% of framework atoms located in stacking faults.[52] The presence of stacking fault domains causes local fault junctures, which are sensitive to dealumination, and hence are regions where mesopores are preferentially generated.[52] Stacking fault domains are randomly distributed in the zeolite and their content may vary depending on the synthesis conditions. In our simulations, we construct stacking fault domains by randomly identifying rectangular units of 1 × 1 × 5 unit cells (with a size of 18.094 × 20.516 × 37.620 Å) as stacking faults. With a probability of 0.8, the stacking fault domain is created at a position where it is connected to a stacking fault domain that was already created. In this way, the size of the resulting mesopores corresponds to those observed in experiments using electron tomography.[38]

2.5. Simulation Scheme for Dealumination. Inspired by the mechanism proposed by Marcilly,[53] our dealumination scheme consists of the following steps (see also Figure 1).

(1) The removal of framework Al (denoted by Al-). Framework Al is removed and transformed into extra-framework Al (Al_{EF}, this typically consists of AlO^+, $Al(OH)^{2+}$ and AlO(OH)). Typically extra-framework Al is removed using a mild acid. In our simulation we only consider the rate of the step to extract Al from the framework, and we assume that all resulting Al_{EF} is effectively removed from the system in a separate step. Due to the hydrolysis of Al-(O−Si-)$_4$ bonds, the removal of one framework Al atom results in the formation of a framework vacancy consisting of four silanol (SiOH) groups, i.e. a silanol nest (here denoted by 4SiOH).

(2) The migration of framework Si (denoted by Si−). Framework Si is mainly extracted from stacking fault domains. The generated Si atoms will migrate through the crystal and eventually heal the generated silanol nests, see below. The migrating Si atoms are denoted by Si_{MG}.

(3) The self-healing of a silanol nest (denoted by Si+). Silanol nests can be healed by migrating Si atoms (Si_{MG}) extracted from stacking fault domains, in order to form a perfect local siliceous structure.

The kinetic Monte Carlo (KMC) method[54] is then used to study the dynamics of the dealumination process. In this method, all possible events (possible simulation steps) are considered and it is assumed that these events are independent. For each T-atom, each of the possible steps are considered as separate events. At each time step, a certain event in the simulation is selected with a probability proportional to its rate r

$$r_{\mathrm{Al}-} = k_{\mathrm{Al}_i}[\mathrm{Al}_i] \quad (1)$$

$$r_{\mathrm{Si}-} = k_{\mathrm{Si}_i}[\mathrm{Si}_i] \quad (2)$$

$$r_{\mathrm{Si}+} = k_{\mathrm{Si}+}[4\mathrm{SiOH}][\mathrm{Si}_{\mathrm{MG}}] \quad (3)$$

in which the brackets [...] denote the concentration of a certain component. For each framework Si or Al atom, the subscript i denotes whether it is connected to 1, 2, 3, or 4 other TO_4 units (where T can be either an Al or Si metal atom). Therefore, the number of hydroxyl group connected to T_i equals $4 - i$. k_{Al_i}, k_{Si_i}, and $k_{\mathrm{Si}+}$ are predetermined rate constants. Note that the Al removal and Si migration are first order reactions, while the self-healing is a second order reaction. The main source of $\mathrm{Si}_{\mathrm{MG}}$ for self-healing originates from stacking fault domains, even though the roughening of the crystal surface and extraction of Si from *Cmcm* domains may also contribute a small amount.[55] As we are only interested in the final zeolite structure after many kinetic Monte Carlo steps, arbitrary units for the reaction rates can be used.

In principle, quantum-mechanical calculations could be used to extract the activation energy and therefore rate constants for the steps given in eqs 1−3. Due to the complexity and heterogeneity of the zeolite framework, this approach is extremely difficult to implement. In our simulations, based on our understanding of the experimental system we have guessed values for these constants as follows. (1) The rate constant of k_{Al_4} is set to 1 (arbitrary units) in the *Cmcm* and stacking fault domain. During dealumination, framework Al is considered to be equally active in both regions. The value of this rate constant is used as a reference for the others. (2) The rate constants are set to a value of 1000 for the following reactants: Al_1, Al_2, Al_3, and Si_1, both in the *Cmcm* and stacking fault domains. The reason for this is that these fragments are not stable. T atoms connected to one or more hydroxyl group are considered less stable during dealumination. As shown by NMR studies, these components hardly exist.[56,57,14,58,59] (3) Rate constants are set to 0 for inert compounds like Si_3 and Si_4. This is reasonable unless hydrofluoric acid is used for dealumination. (4) The rate constant k_{Si_2} in the *Cmcm* region is set to 0.5. This value is between the values for k_{Si_3} and k_{Al_4}. Si_2 is the main component that affects the change of the porosity of the framework. For instance, when $k_{\mathrm{Si}_2} = 0$, silanol nests will be completely healed by $\mathrm{Si}_{\mathrm{MG}}$, resulting in a defect-free framework. For the stacking fault domains, the value of k_{Si_2} is set to a large value (10). (5) As the boundaries between stacking fault domains and *Cmcm* domains are easily destructed, we assume that at these interfaces all Si is as reactive as Al_4 (rate constant of 1). (6) Self-healing of silanol nests is considered to take place equally frequent for all silanol nests, except inside the stacking fault domains where self-healing does not take place as we assume that the Si atoms in these domains will be used for self-healing of the *Cmcm* part of the structure. An overview of all kinetic constants is given in Table 1. The precise values of these parameters is not so important, as long as their relative order of magnitude is reasonable. In our simulations, we assumed that the total fraction of stacking fault domains equals $r_{\mathrm{meso}} = 0.13$ as this results in a similar mesoporosity as in electron tomography experiments. In addition, the value of r_{meso} matches the number of Si atoms needed in the self-healing step in the *Cmcm* domains. In this way, nearly all $\mathrm{Si}_{\mathrm{MG}}$ will be used to heal silanol nests. A typical simulation is started from a large supercell with predefined stacking fault domains. A list of all possible events is constructed, and one of these events is selected with a probability proportional to its rate. After the execution of this event, the list of possible events is updated and the procedure is repeated until the desired Si/Al ratio is reached.

TABLE 1: Rate Constants for Al Removal, Si Migration and Self-Healing (in units of events per unit of time, arbitrary units). The Subscript *i* of a Si/Al Atom Refers to the Number of its Next-Nearest Si/Al Neighbors

Rate Constants for Si Migration, $k_{\mathrm{Si}i}$				
	Si_4	Si_3	Si_2	Si_1
Cmcm domain	0	0	0.5	1000
stacking fault domain	0	0	10	1000
interface	1	1	1	1
Rate Constants for Al Removal, k_{Al_i}				
	Al_4	Al_3	Al_2	Al_1
Cmcm domain	1	1000	1000	1000
stacking fault domain	1	1000	1000	1000
Rate Constants for Self-Healing, $k_{\mathrm{Si}+}$				
Cmcm domain	2			
stacking fault domain	0			

3. Results and Discussion

3.1. Al Distribution. In Figure 2, the Si−Al connectivity as a function of the Si/Al ratio is shown for parent HMOR based on the scheme described in section 2.4. Si(*n*Al) denotes a framework Si atom which is connected via oxygen atoms to n Al atoms ($1 \leq n \leq 4$). In general, for increasing Si/Al ratios the fraction of Si(1Al) and Si(2Al) decreases while the fraction of Si(0Al) increases. The computed fractions of Si(nAl) are in good agreement with available ^{29}Si NMR experiments.[60−62,56,63,57,14,59] The used values for E_{ij} result in a preferential occupation of framework Al at T_3 and T_4 sites,[45] while Al−O−Si−O−Al linkages are unfavorable at the other T sites, following Dempsey's rule. Completely ignoring Dempsey's rule (i.e., $E_{ij}/k_{\mathrm{B}}T = 0$ for each i, j) results in the following distribution: 42% Si(0Al), 42% Si(1Al) and 16% Si(2Al) for MOR with Si/Al= 5, clearly in disagreement with the experimental data in Figure 2. Setting $E_{ij}/k_{\mathrm{B}}T = 10$ for all i,j exactly corresponds to Dempsey's rule. As expected, the resulting fractions of Si(nAl) clearly disagree with the experimental ones

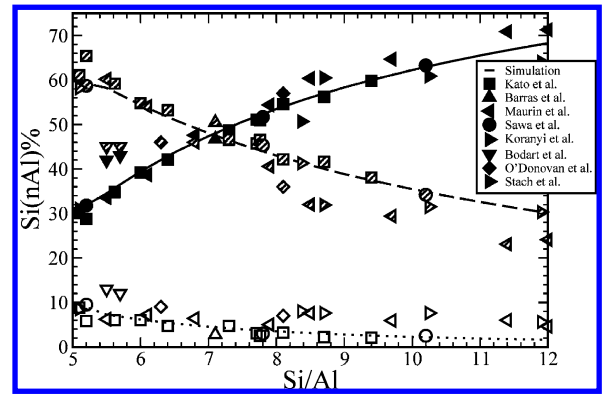

Figure 2. Simulated Si(nAl) distribution of parent HMOR (prior to dealumination). For the ^{29}Si NMR experiments: filled symbols, Si(0Al); semiopen symbols, Si(1Al); open symbols, Si(2Al). For our simulations: solid line, Si(0Al); dash line, Si(1Al); dotted line, Si(2Al). The experimental data is taken from Kato et al.,[60] Barras et al.,[61] Maurin et al.,[62] Sawa et al.,[56] Koranyi et al.,[63] Bodart et al.,[57] O'Donovan et al.,[14] and Stach et al.[59]

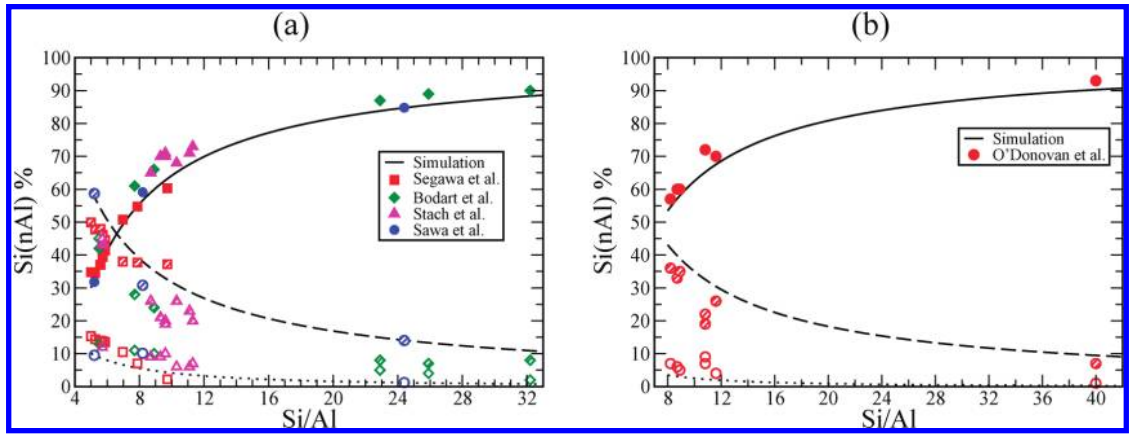

Figure 3. Simulated Si(*n*Al) distributions during dealumination of (a) parent HMOR with Si/Al = 5 and (b) parent HMOR with Si/Al = 8. Experiments: solid symbols, Si(0Al); semiopen symbols, Si(1Al); open symbols, Si(2Al). Simulations: solid line, Si(0Al); dashed line, Si(1Al); dotted line, Si(2Al). The experimental data is taken from Sawa et al.,[56] Bodart et al.,[57] O'Donovan et al.,[14] Segawa et al.,[58] and Stach et al.[59]

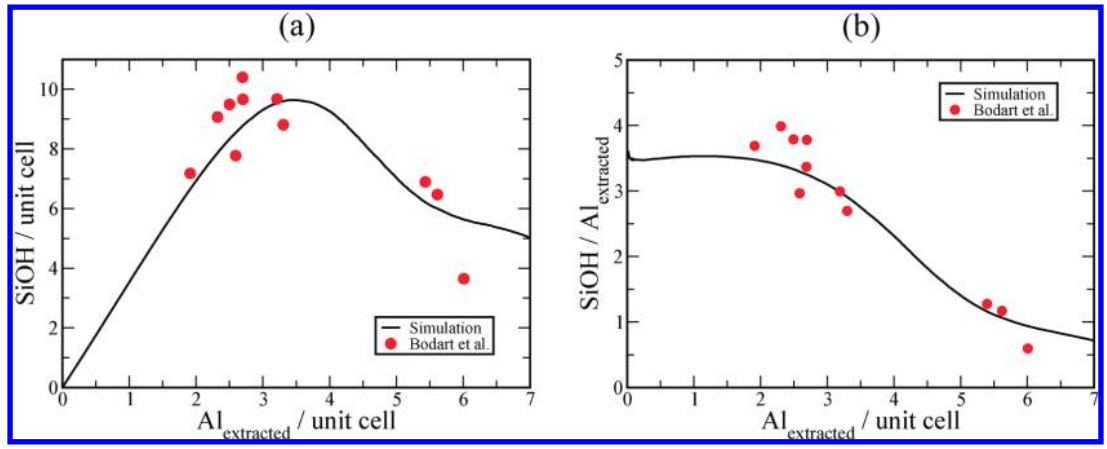

Figure 4. Computed SiOH concentration during dealumination of parent HMOR with Si/Al = 5.5 compared to the experiments by Bodart et al.[57] A ratio of Si/Al= 50 corresponds to ≈6 extracted Al atoms per unit cell.

(data not shown). Therefore, we conclude that Dempsey's rule is valid for all the building units of MOR except for the four-membered ring. We speculate that these findings are also applicable to the other aluminosilicate zeolites with similar secondary building units.

Figure 3 shows the computed fractions of Si(nAl) of dealuminated HMOR based on the dealumination scheme described in section 2.5. The parent HMOR samples have Si/Al ratios of 5 and 8 and are generated using the procedure of section 2.5. Similar trends of the fractions of Si(*n*Al) as a function of the Si/Al ratio can be observed as for parent HMOR (Figure 2). Our simulations are in very good agreement with various ^{29}Si NMR experiments from literature, even though the computed fractions of Si(0Al) and Si(2Al) are slightly lower than the corresponding experimental values, and the computed fraction of Si(1Al) is somewhat larger. We found this is a general trend independent of the precise values of the model parameters of our dealumination scheme. These minor discrepancies can be attributed to the approximations made in the experiments. In ^{29}Si NMR measurements, it is often assumed that the only silanol present in the zeolite framework is SiOH (attributed to peak at −105 ppm) so that the peak at −99 ppm is only caused by Si(2Al) rather than $Si(OH)_2$.[57] However, the Si−Al connectivity of parent HMOR (Figure 2) shows that approximately 10% of the framework Si is present as Si(2Al). During dealumination, Si(2Al) will be quickly transferred into $Si(OH)_2$ resulting in a contribution to the NMR signal at −99 ppm. It is straightforward to show that neglecting the contribution of $Si(OH)_2$ to the NMR signal at −99 ppm will result in an overestimation of the fraction of Si(2Al) and an underestimation of the fraction of Si(1Al) in HMOR.

The concentrations of silanol groups in dealuminated HMOR are shown in Figure 4. Starting from parent HMOR with Si/Al = 5.5, dealuminated HMOR shows a maximum silanol concentration at around three extracted Al atoms per unit cell, in agreement with the available experiments. The change in the number of silanol groups during dealumination indicates that the dealumination process consists of three stages. During the first stage, two dominating reactions take place simultaneously: the removal of framework Al, and the migration of Si at the interface between the stacking fault and *Cmcm* domains. As four SiOH are generated by extracting a single Al atom, the initial slope of Figure 4a should be close to four. A close inspection of our simulation results reveals that this slope is approximately 3.5 SiOH per extracted Al per unit cell. The reason for this difference is that only SiOH is taken into account here. When the number of extracted Al atoms per unit cell reaches around three, the fraction of SiOH rapidly levels off at about ten SiOH per unit cell. Further dealumination results in a decrease of the number of silanol groups. This phenomenon is caused by the self-healing of silanol nests by migrating Si atoms. It is often observed experimentally that dealumination is accompanied by the formation of internal mesopores as well as the roughening of the zeolite external surface.[55] The extracted Si from the stacking fault domains will be used in the self-healing process. The rate constant of self-healing has a larger value than that of Al removal (Table 1). According to eq 3, the self-healing rate is increased significantly when enough migrated

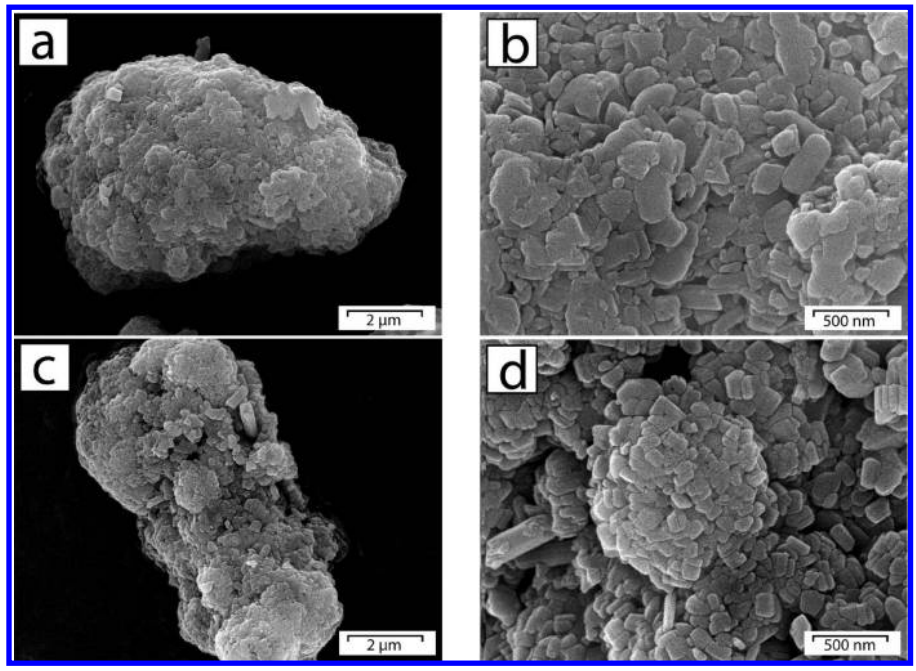

Figure 5. SEM images of (a and b) A6 and (c and d) A50 HMOR samples.

Si is extracted from the stacking fault domains. In the final stage, nearly all framework Al is extracted and the concentration of SiOH levels off at around five SiOH per unit cell. Our simulation shows a good agreement with the experimental data of Bodart et al.[57]

3.2. Changes in Morphology and Crystallinity. Figure 5 shows SEM images of parent and dealuminated mordenite. The images clearly show that particles of a few μm are present, consisting of aggregates of crystallites with typical dimensions of around 200 nm. The dealumination process hardly affects the morphology of the particles, although after dealumination the particles appear to be slightly more open with less densely packed crystallites.

Figure 6 shows the experimental XRD patterns as well as those derived from the simulations, both for parent and dealuminated samples. The parent material was assumed to have a crystallinity of 100%, calculated from the sum of intensities of the peaks defined in section 2.2. Upon dealumination the intensity of the peaks at high diffraction angles decreased both in experiments and simulations. This indicates that the framework is partially dissolved upon dealumination. Note that in experiments the increase in intensities of the peaks at low diffraction angles after dealumination is related to the enhanced hydrophobicity due to the loss of acid sites. This effect is not visible in the simulated spectra, as water was not considered in our simulations. The simulated crystallinity as a function of the degree of dealumination is shown in Figure 7. It is clear that even after heavy dealumination, still 70% crystallinity is retained. Experimentally a crystallinity of 89% was found for A50 sample. This qualitatively agrees with literature reports on the crystallinity of dealuminated MOR and zeolite Y.[14,64,65] In conclusion, the crystallinity and morphology of mordenite crystals are largely preserved upon dealumination, supported by good agreement between experimental and simulation results.

3.3. Impact of Dealumination on the Porosity. The porosity of mordenite before and after dealumination was experimentally analyzed using N_2 and Ar physisorption isotherms, see Figure 8. The N_2 isotherms show a significant uptake at relative pressures below 0.05 due to micropore filling, and a modest hysteresis loop at relative pressures higher than 0.4 indicative of the presence of mesopores.[32−35] The forced closure of the desorption branch of the isotherm around $p/p_0 = 0.4$ indicates that the mesopores can be accessed via openings smaller than about 4 nm. The experimental isotherms suggest a clear increase in both micro- and mesopore volume upon dealumination. In addition, the external surface area is enlarged, which can be attributed to the enlarged mesoporosity and surface roughness during the acid treatment (as was also suggested from the SEM images, Figure 5). Similar results were derived from the Ar physisorption isotherms at high relative pressures. The Ar adsorption isotherms at low pressures give more detailed information on the change of microporosity upon dealumination. In the relative pressure range of $10^{-5}\sim10^{-4}$, the Ar loading in A6 is higher than for A50, while the opposite is true starting from a relative pressure of 10^{-3}. The enlargement of the micropores upon dealumination weakens the adsorption strength, resulting in a low Ar loading at low pressures. This is a typical example for which classical methods of micropore size analysis are not suitable, and it is imperative to use NLDFT to interpret the experimental results. These micropore results of the NLDFT analysis will be compared in detail with simulations.

The simulated pore size distribution of parent mordenite is shown in Figure 9a. Three major peaks are observed at pore diameters of 6.7, 5.1, and 3.8 Å, corresponding to the main channels, the side pockets, and the inaccessible eight-membered channels, respectively. The simulated pore sizes are in excellent agreement with the values reported by the Atlas of Zeolite Framework Types.[39] The various pores in parent mordenite are illustrated in Figure 9b. The computed micropore volume of 0.21 mL/g for micropores of 4.5−8 Å is in good agreement with experimental results considering a 0.01−0.02 mL/g error in the experimentally obtained micropore volume (see table 2). Furthermore, we may expect small differences because of the definition of pore volume in the simulations (section 2.3). After dealumination, the total micropore volume of dealuminated HMOR with Si/Al = 50 is 0.21 mL/g for micropores smaller than 8 Å, identical to that of parent mordenite. This is slightly larger than the experimentally measured micropore volumes (0.20 mL/g measured by N_2 and 0.16 mL/g by Ar physisorption). For dealuminated mordenite, the simulated total pore volume

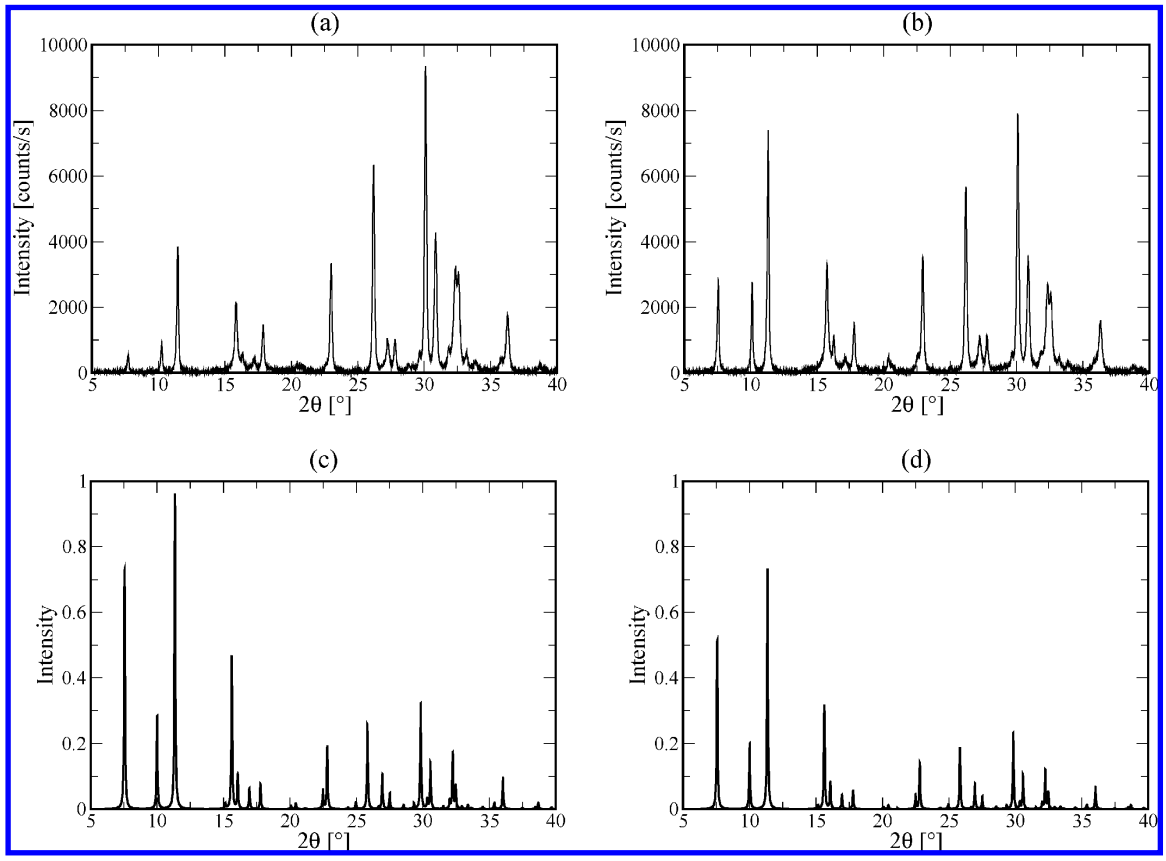

Figure 6. Experimental CoK_α XRD patterns of (a) A6 and (b) A50 HMOR samples. The A50 HMOR has a 89% crystallinity, assuming 100% crystallinity for A6 HMOR. Computed Co Kα XRD powder pattern of (c) parent HMOR with Si/Al = 6.0 and (d) dealuminated HMOR with Si/Al = 50 starting from parent HMOR with Si/Al = 6.0. The latter system has a crystallinity of 72%. The simulated MOR supercell consists of 28 × 25 × 68 unit cells. It is assumed that water is not present. Note that the same scale of the XRD intensities is used for either experiments (a and b) or simulations (c and d).

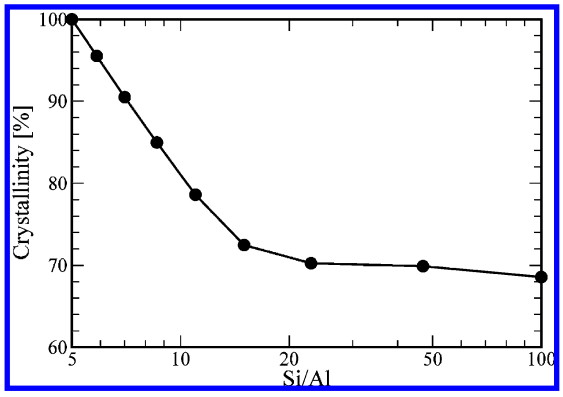

Figure 7. Computed zeolite crystallinity during dealumination of parent HMOR with Si/Al = 5.5.

is 0.297 mL/g. The sum of the mesopore volume and supermicropore volume equals 0.087 mL/g. This is slightly larger than the corresponding values obtained from N_2 and Ar physisorption (both 0.05 mL/g).

Figure 10 shows the influence of dealumination on the micropore size distribution for both the simulations and the analysis of Ar adsorption isotherms. As the experiments result in data with a much lower resolution than in the simulations, the simulation results were binned to a resolution of 0.3 Å to allow a direct comparison. In the parent sample, the micropores in the side pockets and main channels of HMOR are identified as pores of 4.6 and 5.5 Å by the NLDFT method, and as pores of 5.2 and 6.7 Å by simulations. Ar physisorption underestimates pore sizes, which is inherent to probing small pores using Ar atoms with a comparable size. During dealumination, the pore sizes are hardly changed (also see table 2). It is important to note that for both approaches, after dealumination broad peaks can be observed at the pore diameters larger than the main channel of parent mordenite. This indicates a transformation of the main channels upon dealumination. It is clear that much information is lost by the 0.3 Å resolution. However, the direct comparison between simulated and experimental data confirms the validity of our simulation model.

Figure 11a illustrates the importance of our simulations, as information on the micropore size distribution can be obtained with a much higher resolution and detail than is available from experiments. Several conclusions concerning the effect of the dealumination can be drawn:

(1) The peak at a pore size of 3.8 Å which is associated with the modulating eight-membered channel slightly broadens, and the total pore volume associated with this peak does not change significantly.

(2) The peak related to a pore size of 5.1 Å, which is associated with the side pockets, also broadens and its maximum shifts to slightly smaller pore sizes. This is typically caused by the roughing of the side pockets during dealumination. At the same time the total pore volume related to these side pockets significantly decreases (with 0.006 mL/g). This indicates that indeed part of the side pockets is affected by the dealumination process.

(3) The peak at 6.7 Å, which is associated with the main channel, also broadens and shifts to slightly smaller pore sizes. More importantly, also here a significant loss in the total pore volume is observed (of 0.013 mL/g). This loss of the pore

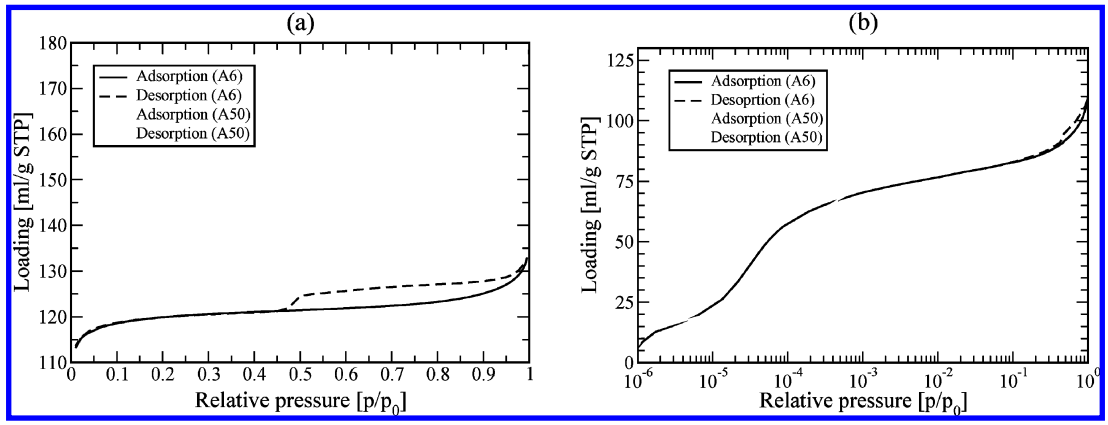

Figure 8. Physisorption isotherms of (a) N_2 and (b) Ar for A6 and A50 HMOR samples.

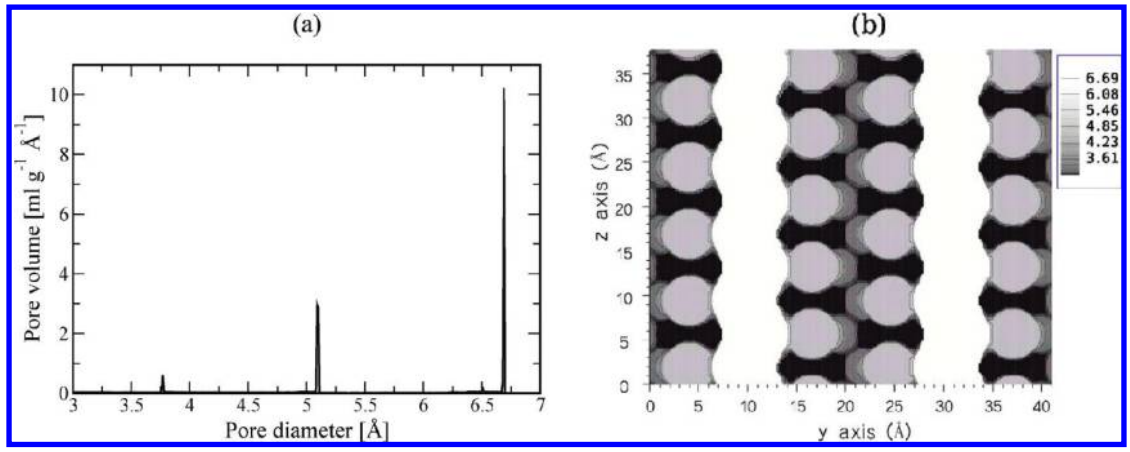

Figure 9. (a) Computed micropore size distribution of parent HMOR Si/Al= 6. (b) Slice through the $y-z$ plane at $x = a/2$, showing the location of the main channels (along the z direction, in white) and the side pockets (gray spherical cavities). The color coding shows the pore diameter in Å. Only pores larger than 3 Å are shown.

TABLE 2: Porosity of A6 and A50 HMOR Samples Analyzed by the NLDFT Method Based on High-Resolution Ar Physisorption Isotherms (Denoted by Ar), N_2 Physisorption (Denoted by N_2), and Simulations (Denoted by sim.)[a]

		A6			A50		
		Ar	N_2	sim.	Ar	N_2	sim.
pore volume [mL/g]	ultramicropore	0.15		0.21	0.16		0.21
	supermicropore	0.00		0	0.01		0.047
	micropore volume	0.15	0.17	0.21	0.17	0.20	0.257
	mesopore	0.03	0.02	0	0.04	0.05	0.04
surface area [m^2 /g]	ultramicropore	1160			1200		
	supermicropore	0			43		
	mesopore	16	26		20	74	
	surface area	1176			1263		
pore diameter [Å]	side pocket	4.62		5.1	4.62		5.0
	main channel	5.52		6.7	5.82		6.6
	secondary pore			0			7.1

[a] In this table, we used the following definitions: ultramicropores are defined as pores smaller than 8 Å, supermicropores are defined as pores of 8−20 Å, mesopores are defined as pores larger than 20 Å, and micropores are defined as pores smaller than 20 Å.

volume is attributed to the destruction of well-defined main channels by dealumination.

(4) After dealumination there is an additional broad peak around pore diameters of 7−7.5 Å. The occurrence of this peak corresponds to newly created pores, significantly larger than the main channels, which has been reported in several experiments.[66,21] The volume of these secondary pores (of 0.016 mL/g) compensates largely for the loss of pore volume associated with the side pockets (of 0.006 mL/g) and main channel (of 0.013 mL/g) upon dealumination. This means that the total micropore volume does not change much upon dealumination.

Concluding, during dealumination, two distinct areas of mordenite are predominantly dissolved: the Al-rich four-membered rings and the internal surfaces of the main channels. This leads to parts of the main channel merging with damaged side pockets nearby (see Figure 11b). Hence part of the pore volume associated with well-defined main channels and side pockets is lost, but secondary pores are formed instead during dealumination. Although in much less detail, these results are validated by the analysis of the Ar physisorption (Figure 10a) which shows pores in the range of 6.1−6.8 Å appearing. We therefore confirm that dealumination of HMOR brings about the formation of the

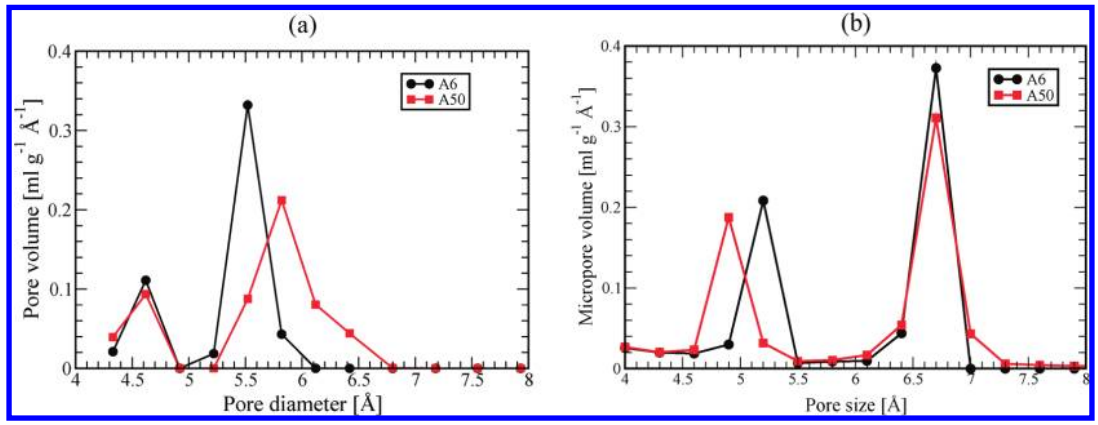

Figure 10. Comparison between (a) the micropore size distribution obtained from Ar physisorption and (b) simulated micropore size distribution for parent HMOR A6 and dealuminated HMOR A50. The parent HMOR A6 has a Si/Al ratio 6, while dealuminated HMOR A50 has a Si/Al ratio 50. The simulated results are obtained by binning the micropore size distribution of Figure 11a.

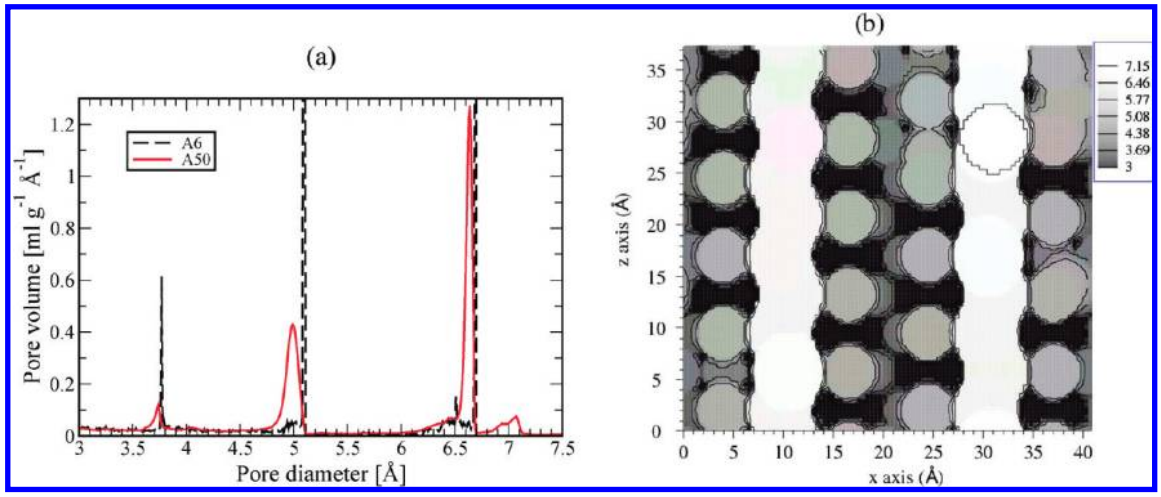

Figure 11. (a) Simulated micropore size distribution of dealuminated HMOR with Si/Al = 50. The micropore size distribution of parent HMOR is taken from Figure 9a and the peaks are not complete shown in this figure. (b) Slice through the $y-z$ plane at $x = a/2$, showing the location of the main channels (along the z direction, in white) and the side pockets (gray spherical cavities). The color coding shows the pore diameter in Å. Only pores larger than 3 Å are shown.

secondary pores in evidence of both simulations and the NLDFT analysis.

4. Conclusions

In this work, we have combined experiments with simulations to achieve a detailed understanding of the effect of dealumination on the pore system of HMOR.

A simulation method is developed to model the distribution of the framework Al in parent HMOR. In agreement with NMR experiments, we can conclude that (1) beside the Löwenstein's rule, the Al content in the four T sites is given by Alberti et al., and[40] (2) Dempsey's rule is valid for all building units of MOR except for the four-membered rings. This leads to the conclusion that the presence of Al stabilizes four-membered rings. This is expected to be valid for other zeolites containing similar building units. For instance, DDR-type zeolites contain no four-membered rings, and thus an all-silica structure can easily be obtained.

In our simulations, dealumination is considered as a multiple-step process consisting of the removal of framework Al and the self-healing of the SiOH nests by migrated Si atoms. The computed Si−Al connectivities agree well with ^{29}Si NMR experiments from literature for both parent and dealuminated HMOR. The SiOH concentration of HMOR during dealumination reveals that the dealumination procedure contains three stages: (1) the removal of framework Al takes place in the *Cmcm* and stacking fault domains simultaneously. In particular, the extraction of the framework Al generates SiOH nests, and migrating Si atoms are created by the removal of the framework Si from the interfaces between the *Cmcm* and stacking fault domains. (2) Once enough SiOH nests and migrating Si atoms are present, the self-healing reaction occurs rapidly to transform some SiOH nests into a silicious structure. (3) The final structure of dealuminated HMOR shows modified micropores and newly created mesopores. All migrating Si atoms are used in the self-healing process. This dealumination mechanism is expected to be applicable to other aluminosilicate zeolites. For example, during dealumination, the Al-rich LTA-type zeolite will be completely dissolved, while MFI-type zeolite may still maintain the well-defined micropores apart from the formation of mesopores. We speculate that this is because of the presence of four-membered rings in LTA-type zeolite, while these rings are absent in MFI-type zeolite.

Ar physisorption experiments are combined with simulation techniques to investigate the microporosity of MOR at the molecular level. For dealuminated MOR, both approaches indicate the formation of the secondary pores (larger than the main channel) in the dealuminated HMOR. The mechanism of this transformation follows from the observation that during dealumination, two distinct areas of the MOR framework are

mainly dissolved: the Al-rich four-membered rings and the internal surfaces of the main channels. This results in merging of the main channels with damaged side pockets nearby, forming large secondary pores during dealumination. Such an enlargement of micropores may have a considerable effect on the catalytic performance of MOR.

Acknowledgment. The authors acknowledge funding from the ACTS/ASPECT program from The Netherlands Organization for Scientific Research (NWO−CW). T.J.H.V. and P.E.d.J. acknowledge financial support from NWO through VIDI grants. We would like to thank Dr. Gerbrand Mesu from Albemarle Catalysts for supplying the mordenite samples.

References and Notes

(1) Davis, M. E. *Nature* **2002**, *417*, 813–821.
(2) Tao, Y.; Kanoh, H.; Abrams, L.; Kaneko, K. *Chem. Rev.* **2006**, *106*, 896–910.
(3) Egeblad, K.; Christensen, C. H.; Kustova, M.; Christensen, C. H. *Chem. Mater.* **2008**, *20*, 946–960.
(4) van Donk, S.; Janssen, A. H.; Bitter, J. H.; de Jong, K. P. *Catal. Rev.—Sci. Eng.* **2003**, *45*, 297–319.
(5) Pérez-Ramírez, J.; Christensen, C. H.; Egeblad, K.; Christensen, C. H.; Groen, J. C. *Chem. Soc. Rev.* **2008**, *37*, 2530–2542.
(6) Choi, M.; Cho, H. S.; Srivastava, R.; Venkatesan, C.; Choi, D.; Ryoo, R. *Nat. Mater.* **2006**, *5*, 718–723.
(7) Schmidt, I.; Boisen, A.; Gustavsson, E.; Stahl, K.; Pehrson, S.; Dahl, S.; Carlsson, A.; Jacobsen, C. J. H. *Chem. Mater.* **2001**, *13*, 4416–4418.
(8) Jacobsen, C. J. H.; Madsen, C.; Houzvicka, J.; Schmidt, I.; Carlsson, A. *J. Am. Chem. Soc.* **2000**, *122*, 7116–7117.
(9) Tao, Y.; Kanoh, H.; Kaneko, K. *J. Am. Chem. Soc.* **2003**, *125*, 6044–6045.
(10) Groen, J. C.; Moulijn, J. A.; Pérez-Ramírez, J. *J. Mater. Chem.* **2006**, *16*, 2121–2131.
(11) Ogura, M.; Hinomiya, S.; Tateno, J.; Nara, Y.; Kikuchi, E.; Matsukata, M. *Chem. Lett.* **2008**, *8*, 882–883.
(12) Lee, G. S.; Maj, J. J.; Rocke, S. C.; Garcés, J. M. *Catal. Lett.* **1989**, *2*, 243–248.
(13) Lee, G. J.; Graces, J. M.; Meima, G. R.; van der Aalst, M. J. M. *U.S. Patent 5,198,595*, 1991.
(14) O'Donovan, A. W.; O'Connor, C. T.; Koch, K. R. *Micropor. Matt.* **1995**, *5*, 185–202.
(15) Ivanova, I. I.; Montouillout, V.; Fernandez, C.; Marie, O.; Gilson, J. P. *Microporous Mesoporous Mater.* **2003**, *57*, 297.
(16) Weyda, H.; Köhler, E. *Catal. Today* **2003**, *81*, 51–55.
(17) Choudhary, V. R.; Mayadevi, S.; Singh, A. P. *J. Chem. Soc. Faraday Trans.* **1995**, *91*, 2935–2944.
(18) Webster, C. E.; Cottone, A.; Drago, R. S. *J. Am. Chem. Soc.* **1999**, *121*, 12127–12139.
(19) Goovaerts, F.; Vansant, E. F.; Philippaerts, J.; Hulsters, P. D.; Gelan, J. *J. Chem. Soc., Faraday Trans. 1* **1989**, *85*, 3675–3685.
(20) Lin, F. N. Davis, E. D., US patent 6140547, 2000.
(21) Chung, K. H. *Microporous Mesoporous Mater.* **2008**, *111*, 544–550.
(22) Nagano, J.; Eguchi, T.; Asanuma, T.; Masui, H.; Nakayama, H.; Nakamura, N.; Derouane, E. G. *Microporous Mesoporous Mater.* **1999**, *33*, 249–256.
(23) Tromp, M.; van Bokhoven, J. A.; Oostenbrink, M. T. G.; Bitter, J. H.; de Jong, K. P.; Koningsberger, D. C. *J. Catal.* **2000**, *190*, 209.
(24) Hunger, B.; Heuchel, M.; Clark, L. A.; Snurr, R. Q. *J. Phys. Chem. B* **2002**, *106*, 3882–3889.
(25) Chandra, A. K.; Goursot, A.; Fajula, F. *J. Mol. Catal. A: Chem.* **1997**, *119*, 45–50.
(26) Viswanadham, N.; Kumar, M. *Microporous Mesoporous Mater.* **2006**, *92*, 31–37.
(27) Sokol, A. A.; Catlow, C. R. A.; Garces, J. M.; Alex Kuperman, A. *J. Phys. Chem. B* **2002**, *106*, 6163–6177.
(28) Datong Ding, D. T.; Sun, P. C.; Jin, Q. H.; Li, B. H.; Wang, J. Z. *Zeolites* **1994**, *14*, 65–73.
(29) Treacy, M. M. J.; Higgins, J. B. *Collection of Simulated XRD Powder Patterns for Zeolites*, 7th ed.; Elsevier Science: Amsterdam, 2007.
(30) Waasmaier, D.; Kirfel, A. *Acta Cryst. A* **1995**, *51*, 416–431.
(31) Neimark, A. V.; Ravikovitch, P. I.; Grun, M.; Schüth, F.; Unger, K. K. *J. Colloid Interface Sci.* **1998**, *207*, 159–169.
(32) Neimark, A. V.; Ravikovitch, P. I. *Microporous Mesoporous Mater.* **2001**, *44−45*, 697–707.
(33) Ravikovitch, P. I.; Neimark, A. V. *Langmuir* **2002**, *18*, 1550–560.
(34) Smarsly, B.; Thommes, M.; Ravikovitch, P. R.; Neimark, A. V. *Adsorption* **2005**, *11*, 653–655.
(35) Thommes, M.; Smarsly, B.; Groenewolt, M.; Ravikovitch, P. I.; Neimark, A. V. *Langmuir* **2006**, *22*, 756–764.
(36) Ban, S.; Vlugt, T. J. H. *Mol. Sim.* **2009**, *35*, 1105–1115.
(37) Cejka, J., van Bekkum, H., Corma, A., Schüth, F. Eds.; *Introduction to Zeolite Science and Practice*, 3rd ed.; Elsevier: Amsterdam, 2007.
(38) Koster, A. J.; Ziese, U.; Verkleij, A. J.; Janssen, A. H.; de Jong, K. P. *J. Phys. Chem. B* **2000**, *104*, 9368.
(39) Baerlocher, C.; McCusker, L. B.; Olson, D. H. *Atlas Of Zeolite Framework Types*; Elsevier: Amsterdam, 2007.
(40) Alberti, A. *Zeolites* **1997**, *19*, 411–415.
(41) Lu, B. W.; Kanai, T.; Oumi, Y.; Sano, T. *J. Porous Mater.* **2007**, *14*, 89–96.
(42) Yuan, S. P.; Wang, J. G.; Li, Y. W.; Peng, S. Y. *J. Molec. Catal. A: Chemical* **2001**, *175*, 131–138.
(43) Oumi, Y.; Kanai, T.; Lu, B. W.; Sano, T. *Microporous Mesoporous Mater.* **2007**, *101*, 127–133.
(44) Brändle, M.; Sauer, J. *J. Am. Chem. Soc.* **1998**, *120*, 1556–1570.
(45) García-Pérez, E.; Dubbeldam, D.; Liu, B.; Smit, B.; Calero, S. *Angew. Chem.* **2007**, *46*, 276–278.
(46) Liu, B.; García-Pérez, E.; Dubbeldam, D.; Smit, B.; Calero, S. *J. Phys. Chem. C* **2007**, *11*, 10419–10426.
(47) Dempsey, E. *Mol. Sieves Soc. Chem. Ind., London* **1968**, p. 293.
(48) Schröder, K. P.; Sauer, J. *J. Phys. Chem.* **1993**, *97*, 6579.
(49) Limtrakul, J.; Yoinuan, J.; Tantanak, D. *J. Mol. Struct. (Theochem)* **1995**, *332*, 151–159.
(50) Limtrakul, J.; Tantanak, D. *Chem. Phys.* **1996**, *208*, 331–340.
(51) Takaishi, T.; Kato, M.; Itabashi, K. *J. Phys. Chem.* **1994**, *98*, 5742–5743.
(52) Rudolf, P. R.; Garces, J. M. *Zeolites* **1994**, *14*, 137–147.
(53) Marcilly, C. R. *Pétrole Tech.* **1986**, *328*, 12–18.
(54) Chatterjee, A.; Vlachos, D. G. *J. Comput.-Aided Mater. Des.* **2007**, *14*, 253–308.
(55) Giudici, R.; Kouwenhoven, H. W.; Prins, R. *App. Catal. A: General* **2000**, *203*, 101–110.
(56) Sawa, M.; Niwa, M.; Murakami, Y. *Zeolites* **1990**, *10*, 532.
(57) Bodart, P.; Nagy, J. B.; Debras, G.; Gabelica, Z.; Jacobs, P. A. *J. Phys. Chem.* **1986**, *90*, 5183–5190.
(58) Segawa, K.; Shimura, T. *App. Catal. A: General* **2000**, *194−195*, 309–317.
(59) Stach, H.; Janchen, J.; Jerschkewitz, H. G.; Lohse, U.; Parlitz, B.; Zibrowius, B. *J. Phys. Chem.* **1992**, *96*, 8473–8479.
(60) Kato, M.; Itabashi, K.; Matsumoto, A.; Tsutsumi, K. *J. Phys. Chem. B* **2003**, *107*, 1788–1797.
(61) Barras, J.; Klinowshi, J.; McComb, D. W. *J. Chem. Soc. Faraday Trans.* **1994**, *90*, 3719–3723.
(62) Maurin, G.; Senet, P.; Devautour, S.; Henn, F.; van Doren, V. E.; Giuntin, J. C. *J. Phys. Chem. B* **2001**, *105*, 9157–9161.
(63) Koranyi, T. I.; Nagy, J. B. *J. Phys. Chem. B* **2005**, *109*, 15791–115797.
(64) Janssen, A. H.; Koster, A. J.; de Jong, K. P. *Angew. Chem., Int. Ed.* **2001**, *40*, 1102–1104.
(65) Wang, Q. L.; Giannetto, G.; Torrealba, M.; Perot, G.; Kappenstein, C.; Guisnet, M. *J. Catal.* **1991**, *130*, 459–470.
(66) Meima, G. R. *Cattech* **1998**, *2*, 5–12.

JP909900A